Published in final edited form as:

Nat Chem Biol. 2009 April ; 5(4): 251–257. doi:10.1038/nchembio.153.

Transition state analogues of 5′-methylthioadenosine nucleosidase disrupt quorum sensing

Jemy A. Gutierrez, **Tamara Crowder**, **Agnes Rinaldo-Matthis**, **Meng-Chiao Ho**, **Steven C. Almo**, and **Vern L. Schramm***

Department of Biochemistry, Albert Einstein College of Medicine, 1300 Morris Park Avenue, Bronx, New York, 10461

SUMMARY

5′-Methylthioadenosine nucleosidase (MTAN) is a bacterial enzyme involved in *S*-adenosylmethionine-related quorum sensing pathways that induce bacterial pathogenesis factors. Transition state analogues 5′-methylthio- (MT-), 5′-ethylthio- (EtT-) and 5′-butylthio- (BuT-) DADMe-ImmucillinAs are slow-onset, tight-binding inhibitors of *Vibrio cholerae* MTAN (*Vc*MTAN), with dissociation constants of 73, 70, and 208 pM, respectively. Structural analysis of *Vc*MTAN with BuT-DADMe-ImmucillinA reveals interactions contributing to the high affinity. In *V. cholerae* cells, these compounds are potent MTAN inhibitors with IC_{50} values of 27, 31, and 6 nM for MT-, EtT-, and BuT-DADMe-ImmucillinA, disrupting autoinducer production in a dose-dependent manner without affecting growth. MT- and BuT-DADMe-ImmucillinA also inhibit autoinducer-2 production in enterohemorrhagic *Escherichia coli* O157:H7 with IC_{50} values of 600, and 125 nM, respectively. BuT-DADMe-ImmucillinA inhibition of autoinducer-2 production in both strains persists for several generations, and causes reduction in biofilm formation. These results support MTAN's role in quorum sensing, and its potential as target for bacterial anti-infective drug design.

Bacteria communicate to each other by a process known as quorum sensing. When the population density reaches critical levels, they produce and detect signaling molecules known as autoinducers (AIs) to coordinate gene expression and regulate processes beneficial to the microbial communities1. With the growing global threat of multi-drug resistance, nonconventional anti-infective discovery approaches are being explored that are nonlethal to bacteria where the potential to develop resistance is assumed to be less significant. Quorum sensing is an ideal target for bacterial anti-infective design, as many bacterial species use this mechanism to regulate virulence2–5. Several mutant bacterial strains defective in quorum sensing create less potent infections. Quorum sensing-deficient intranasal *Streptococcus pneumoniae* infections in mouse are less effective at spreading to the lungs or the bloodstream6. In an infant rat *Neisseria meningitidis* infection model, a quorum sensing-deficient strain is unable to produce viable bacteria in the blood7. These findings, among

*Corresponding author: Vern L. Schramm, Telephone (718) 430-2813, Fax (718) 430-8565, Email vern@aecom.yu.edu.

others, suggest that a number of bacterial infections could be controlled by impeding quorum sensing.

5′-Methylthioadenosine/*S*-adenosyl homocysteine nucleosidases (MTANs) play a crucial role in maintaining homeostasis in bacteria. MTANs are tightly linked to *S*-adenosyl methionine pathways that involve methylation reactions yielding *S*-adenosyl homocysteine (SAH, **1**), and polyamine biosynthesis producing methylthioadenosine (MTA, **2**) (Fig. 1). MTANs catalyze the hydrolytic deadenylation of MTA and SAH and provide the only known route for their metabolism in bacteria, whose accumulation is expected to inhibit related pathways. In addition, MTANs are directly involved in the biosynthesis of autoinducers. AI-1 and AI-2 are two classes of autoinducers synthesized from *S*-adenosyl methionine (SAM, **3**) (Fig. 1). AI-1 is a family of acyl-homoserine lactones (AHLs, such as hydroxy-butanoyl-L-homoserine lactone, **4**) **[Au: edit ok, as compound 4 cannot be a class of chemicals?]** believed to provide signaling molecules for intra-species communication. AI-2 includes derivatives of 4,5-dihydroxy-2,3-pentanedione (DPD, **5**), responsible for inter-species communication. Thus, MTAN inhibition may provide a method of blocking both AI-1 and AI-2 production, and thereby disrupting quorum sensing.

MTAP or 5′-methylthioadenosine phosphorylase is the counterpart to MTAN in humans, and functions similarly in metabolizing MTA but uses phosphate as a nucleophile instead of water. MTAP has been identified as an anticancer target due to its involvement in polyamine biosynthesis, purine and *S*-adenosylmethionine salvage pathways8,9. The transition state structures of human MTAP as well as MTANs from *Escherichia coli* (*Ec*MTAN), *Streptococcus pneumoniae* (*Sp*MTAN), and *Neisseria meningitidis* (*Nm*MTAN) have been solved using kinetic isotope effects10–13. They all have dissociative S_N1 transition states with ribooxacarbenium ion character, which could either be “late” transition states with fully broken *N*-glycosidic bonds (*i.e.*, C1′-N9 distance of 3.0 Å or greater), or “early” transition states with C1′-N9 distances of 2.0 Å or less (Fig. 2a).

Transition state analysis provides blueprints for the design of stable analogues, which in the study of purine nucleoside phosphorylases, has yielded extremely potent inhibitors currently in clinical trials for autoimmune disease and cancer14,15. The same drug design approach has been extended to MTAP and MTANs10–13. Derivatized ImmucillinA (ImmA) and DADMe-ImmucillinA (DADMe-ImmA) provide two generations of transition state analogues developed for MTAP and MTANs16,17. ImmA derivatives mimic early dissociative transition states, while DADMe-ImmA derivatives resemble late dissociative transition states (Fig. 2a,b). The cationic N1′ of DADMe-ImmA resembles the cationic C1′ of the ribosyl group in late, dissociative transition states. In addition, the methylene group between 9-deazaadenine and the pyrrolidine ring in DADMe-ImmA provides geometric similarity between the adenine leaving group and the ribooxacarbenium site, and the 9-deazaadenine provides chemical stability and mimics the increased pKa at N7 found at the MTAN transition states.

ImmA and DADMe-ImmA derivatives synthesized and tested against MTAP and MTANs exhibit some of the highest affinities ever achieved for noncovalent enzyme-inhibitor interactions18–21. For instance, para-chloro-phenylthio-DADMe-ImmA (**6**) inhibits purified

*Ec*MTAN with a dissociation constant of 47 fM, approaching a K_m/K_i ratio of ~10^8 18. Methylthio-DADMe-ImmA (**7**) inhibits purified human MTAP with 86 pM affinity, and induces apoptosis in cultured head and neck squamous cell carcinoma cell lines without affecting normal human fibroblast cell lines9. It also suppresses tumor growth in mouse xenografts at doses nontoxic to the animals9. The bioavailability and nontoxic properties of methylthio-DADMe-ImmA make this class of compounds valuable drug candidates. We propose that similar analogues for MTAN may be effective in blocking MTAN activity in cells.

The current work provides *in vitro* cell characterization of MTAN inhibition and its role in quorum sensing using transition state analogues. Inhibition of *Vibrio cholerae* MTAN (*Vc*MTAN) activity in recombinant purified enzyme as well as in cell cultures was characterized for the slow-onset, tight-binding DADMe-ImmAs. The effects of these inhibitors on autoinducer production and biofilm formation in pathogenic strains of *V. cholerae* and *E. coli* are also described. The results support MTAN's role in quorum sensing, and indicate that MTAN may be an important target for drug design in anti-infective therapies.

RESULTS

MTAN transition state analogues are picomolar inhibitors of *Vc*MTAN

*Vc*MTAN has substrate specificity for hydrolysis of both MTA and SAH. We obtained a K_m of 3 μM for MTA and a k_{cat} of 2 s^{-1}. For SAH, the K_m and k_{cat} values were 24 μM, and 0.5 s^{-1}, respectively. With a k_{cat}/K_m ratio of 6.6 × 10^5 $M^{-1}s^{-1}$ for MTA, *Vc*MTAN's catalytic efficiency was 60-fold greater than the *S. pneumoniae* isoform, and 14-fold less than for *E. coli* MTAN18,20. The transition state analogues 5′-methylthio-DADMe-ImmucillinA (MT-DADMe-ImmA, **7**), 5′-ethylthio-DADMe-ImmucillinA (EtT-DADMe-ImmA, **8**), and 5′-butylthio-DADMe-ImmucillinA (BuT-DADMe-ImmA, **9**) (Fig. 2b) inhibited *Vc*MTAN activity with dissociation constants in the mid-picomolar range (Table 1), compared to *E. coli* MTAN in the low picomolar, and to *S. pneumoniae* MTAN in the nanomolar ranges18,20. The same transition state analogues inhibited *Vc*MTAN with an affinity intermediate to that for *E. coli* and *S. pneumoniae* MTANs, as predicted by the catalytic enhancement provided by the enzymes. Reaction progress curves in the presence of various concentrations of MT-, EtT-, and BuT-DADMe-ImmA revealed time-dependent, slow-onset inhibition, yielding overall dissociation constants of 73, 70, and 208 pM, respectively (Supplementary Fig. 1a online).

A method for predicting the transition state structure for MTANs was reported recently, using dissociation constants for known transition state analogues21. This method classifies MTANs as having either early or late dissociative transition states, depending on the ratio of its dissociation constants for 5′-substituted ImmAs and DADMe-ImmAs. Dissociation constants were determined for *Vc*MTAN with methylthio- (**10**), ethylthio-(**11**), benzylthio-(**12**), and para-chloro-phenylthio-ImmucillinA (**13**) (Supplementary Table 1 online). For the MT-ImmA/DADMe-ImmA inhibitor pair, *Vc*MTAN gave a $K_{ImmA}/K_{DADMe\text{-}ImmA}$ of 137, indicating a strong preference for the transition state analogue that resembles a late transition

state. This analysis predicts a late dissociative transition state for *Vc*MTAN, similar to that of *E. coli* and *S. pneumoniae*. In addition to the ImmA dissociation constants being higher than their DADMe-ImmA counterparts, there was no slow onset phase in their inhibition profiles. Thus, the DADMe-ImmA compounds are better mimics of *Vc*MTAN's transition state, which strongly suggests that it is late and dissociative.

Crystal structure of *Vc*MTAN-BuT-DADMe-ImmA complex

To define the determinants responsible for inhibitor binding, we solved the crystal structure of *Vc*MTAN in complex with BuT-DADMe-ImmA to 2.3 Å resolution (Fig. 3). The final atomic model contained residues 1 – 230 for each monomer of *Vc*MTAN in the asymmetric unit. The largest part of the N-terminal 6-His tag and the last C-terminal residue, 231, were omitted from the structure model due to lack of electron density.

The *Vc*MTAN structure complexed with BuT-DADMe-ImmA had two monomers in the asymmetric unit related by 2-fold noncrystallographic symmetry which corresponds to the functional dimer (Fig. 3a). Density for the inhibitor in the active site was clearly visible at a σ-level of 5, in maps generated after the first round of refinement (Fig. 3b). The structure of the *Vc*MTAN monomer was a single mixed α/β domain with central twisted nine-stranded mixed β-sheet surrounded by six α-helices (Fig. 3a). Both the monomeric structure and the dimeric form were very similar to the MTAN from *E. coli* with rms deviations of 0.44 Å comparing the Cα of the two structures although the sequence identity is only 59% 22. The dimer interface involved hydrophobic residues coming from two α-helices and three loop regions from each monomer.

The catalytic site is situated in a pocket formed by residues from β10, a loop between β8 and α4 and a loop contributed by the adjacent subunit (Fig. 3c). The catalytic site can be divided into three parts, the base binding site, the ribose binding site and the 5′-alkylthio-binding site. The purine base contacts Phe152, main chain atoms of Val153, and side chain of Asp198 (Fig. 3d). Phe152 makes hydrophobic stacking interactions with the 9-deazaadenine base of the inhibitor. The carbonyl oxygen of Val153 accepts a hydrogen bond from the N6 amino group (2.96 Å) of adenine while the amide nitrogen of Val153 donates a hydrogen bond to N1 (3.10 Å). The side chain of Asp198 accepts hydrogen bonds from the N6 amino group (2.89 Å) and NH7 (2.69 Å) of the base. Ser197 hydrogen bonds to $O^{\delta}2$ of Asp198 (2.55 Å) and places the side chain in an orientation favorable for catalysis. The amide nitrogen of Val199 may also orient the Asp198 for catalysis by hydrogen bonding to $O^{\delta}1$ of the latter.

The pyrrolidine moiety participates in interactions with Met9, Phe208 and Met174 on both sides of this ribosyl mimic. The pyrrolidine moiety shares hydrogen bonds with Glu175 and the proposed catalytic water (WAT3) (Fig. 3d). The $O^{\varepsilon}1$ of Glu175 hydrogen bonds to the 3′-hydroxyl of the pyrrolidine with a distance of 2.71 Å. The protonated N1′ nitrogen of the pyrrolidine donates a hydrogen bond to WAT3 (2.73 Å). WAT3 is further stabilized by several hydrogen bonds with $O^{\varepsilon}2$ of Glu175 (2.94 Å), $O^{\varepsilon}1$ and $O^{\varepsilon}2$ of Glu12 (3.41 and 2.91 Å), and NH1 of Arg194 (2.68A). The side chain of Ser76 is also within hydrogen bond distance to $O^{\varepsilon}2$ of Glu12 (2.78 Å) and is involved in holding Glu12 in place for catalysis.

The 5′-butylthio group is surrounded by hydrophobic residues including Met9, Ile50, Val102, Phe105, Ala113, Phe152, Met174, Tyr107 and Phe208 (Fig. 3c). Both subunits form the catalytic site and Tyr107, Phe105, Ala113 and Val102 reside on the adjacent subunit.

Inhibition of cellular MTAN activity

We cultured *V. cholerae* N16961 overnight in the presence of the transition state analogues and saw no effect on cell growth as demonstrated by the invariant OD_{600} at concentrations up to 1 μM, 14,000 times the K_i^* value (Supplementary Fig. 1b online). We took the cleared lysates from washed cells and incubated with radiolabeled MTA, and found MTAN activity from cells cultured without inhibitor to be 89 ± 3 pmol/min/OD_{600} unit, which reflects the variability in the cell density attained by overnight cultures, as well as the amount of active MTAN in extracts. In the presence of the transition state analogues, we saw dose-dependent inhibition of adenine conversion, giving IC_{50}s for the loss of cellular MTAN activity of 27, 31, and 6 nM for MT-, EtT-, and BuT-DADMe-ImmA, respectively (Table 1 and Supplementary Fig. 1c online).

Inhibition of autoinducer production

Under the same conditions used to assay the inhibition of cellular MTAN activity, we measured autoinducer production by *V. cholerae* N16961 as a function of inhibitors (Table 1). *V. cholerae* N16961 growth media induced luminescence in quorum sensing *V. harveyi* reporter strains BB170 and BB120, by a factor of 13.5 (± 4.5), and 2.3 (±1.0), respectively, compared to blank media. BB170 responds to the presence of AI-2 alone, whereas BB120 responds to both AI-1 and AI-2. Marginal induction in BB120 was previously observed for other strains of *V. cholerae* subjected to the same assay23. It was postulated that in the presence of system 1 (response system for AI-1) in *V. harveyi* BB120 strain, system 2 (response system for AI-2) is less sensitive to induction23. MTAN inhibitors caused the AI response signal to become progressively weaker as inhibitor concentration increased, and was completely inhibited at 1 μM (Supplementary Fig. 1d online). We obtained IC_{50} values for suppression of light induction in BB170 of 0.94, 11, and 1.4 nM for MT-, EtT-, and BuT-DADMe-ImmA, whereas in BB120 the IC_{50}s were 10.5, 14, and 1 nM for the same inhibitors (Table 1). Inhibitors alone at concentrations present in AI detection assays, had no effect on light output from the reporter strains, supporting action of the transition state analogues on MTAN of *V. cholerae* cells for their effect on autoinducer production.

Autoinducer production in MTAN$^-$ *E. coli*

We cultured *E. coli* O157:H7 and an MTAN knockout strain in the presence of up to 0.5 μM MT- and BuT-DADMe-ImmA and found no growth defects in AB medium (Supplementary Fig. 2a online). AI induction in BB170 reached 37-fold for the wild-type pathogenic strain compared to blank, while administration of MT- and BuT-DADMe-ImmA resulted in a dose-dependent inhibition of AI-2 induction with an IC_{50} of 600 ± 50 nM, and 125 ± 24 nM, respectively. We found that at only four times the IC_{50} value for BuT-DADMe-ImmA, induction was reduced to 6-fold (Fig. 4a), while the extent of AI-2 induction for the MTAN knockout was negligible. Genetic interruption of MTAN in *E. coli* shows that it is not

essential for growth although it is important for synthesis of quorum sensing molecules. Wild type *E. coli* treated with BuT-DADMe-ImmA produced the same phenotype as the $MTAN^{-}$ strain, supporting MTAN as the target for action of the transition state analogue in the cell.

Persistent suppression of quorum sensing in *E. coli* and *V. cholerae*

Pathogenic strains of *E. coli* and *V. cholerae* maintained sensitivity to BuT-DADMe-ImmA suppression of autoinducer-2 production for sustained growth cycles. With LB as growth medium, *E. coli* O157:H7 achieved 195-fold light induction in the *V. harveyi* BB170 reporter (Fig. 4b). After 26 generations of growth (*i.e.*, 226 expansion of cell number) in the presence of 1 μM or 2.5 μM inhibitor, we saw that light induction in BB170 was suppressed to near basal levels of 1.4- and 2.2- fold, respectively. In *V. cholerae* N16961, the quorum sensing signal after 26 generations was 540-fold relative to control, and showed dramatic inhibition to 4.2- and 1.3 fold, in the presence of 1 μM or 2.5 μM BuT-DADMe-ImmA (Fig. 4c). Again, we observed that growth of both strains remained uninhibited under these conditions (Supplementary Fig. 2b, c online).

Inhibition of biofilm formation

We used a 96-well plate format for the detection of biofilm formation in both *E. coli* O157:H7 and *V. cholerae* N16961. *E. coli* O157:H7 formed biofilm at the bottom of the plate, whereas *V. cholerae* N16961 produced biofilm both at the bottom and at the air-liquid interface. Growth of the planktonic cells reached a modest OD_{600} of 0.5 for *E. coli* and 0.4 for *V. cholerae* under static growth conditions and at 25 ° (Supplementary Fig. 2d, e online), while *V. cholerae* produced three-fold more biofilm than did *E. coli*.

BuT-DADMe-ImmA (1 μM) did not inhibit growth of cells in the assay, but reduced biofilm production by 18% in *E. coli*, and 71% in *V. cholerae* (Fig. 4d, e).

DISCUSSION

The slow-onset, tight-binding inhibition of *Vc*MTAN by MT-, EtT-, and BuT-DADMe-ImmA exhibits some of the highest binding affinities for targets in quorum sensing pathways. Slow onset inhibition is typical for transition state analogues where binding to enzyme equilibrates the protein to a new conformation within seconds to minutes. The enzyme-inhibitor complex is characterized by a slow dissociation rate because of a highly stable inhibited form. K_m/K_i values for all three inhibitors are approximately 10^4, showing strong preference for the transition state analogues over the substrate MTA.

MTANs have dual substrate specificity for MTA and SAH, and are expected to accommodate both methylthio- and homocysteine groups in a manner proportional to their K_m values. Transition state analogues that differ only in their 5′-substituents permit direct comparison of *Vc*MTAN's preference for these groups. MT- and EtT- groups were equally favored at this position, and are also equivalent in blocking quorum sensing *in vitro* (Table 1). The dissociation constant increases three-fold however, in going from ethyl- to butyl-substituted DADMe-ImmA and suggests modest size specificity within the 5′-binding pocket.

The crystal structure of BuT-DADMe-ImmA in complex with *Vc*MTAN is similar to the crystal structure of *Ec*MTAN in complex with MT-DADMe-ImmA (Supplementary Fig. 3a online)22. The inhibitors in the two structures share a virtual overlap of the 9-deazaadenine and the pyrrolidine ribocation mimic. Similar to *Ec*MTAN, tight binding in the *Vc*MTAN complex is proposed to originate mainly from the conformation adopted by the pyrrolidine group of the inhibitor that allows for the cation at N1′ to be in close proximity to the putative water nucleophile which organizes the geometry of Ser76, Glu12, Arg194, and Glu175 around the catalytic site. The pKa of the N1′ pyrrolidine nitrogen is 8, making it cationic at physiological pH. The DADMe-ImmA inhibitors lack the 2′-hydroxyl moiety of ribosyl groups and allow the presumed catalytic water to be close to the N1′ with a distance of 2.7 Å. This distance was similar to the 2.6 Å in the case of the *Ec*MTAN-MT-DADMe-ImmA structure22. Based on the favorable hydrophobic interactions between the 5′-butylthio group and the hydrophobic pocket in the protein, additional binding affinity would be anticipated relative to MT-DADMe-ImmA. The 3-fold decrease in affinity for BuT- inhibitor relative to MT- inhibitor may correspond to the entropy loss upon binding the flexible butyl group at the catalytic site.

BuT-DADMe-ImmA binds 1000 times stronger to the *Ec*MTAN than to the *Vc*MTAN. Comparisons of the structures overall and the active sites do not reveal obvious explanations for the difference (Supplementary Fig. 3a, b online). The two structures share 59% sequence identity and have almost identical active sites. However, recent studies have demonstrated that residues remote from the active site of purine nucleoside phosphorylase contribute to transition state structure and catalytic efficiency through dynamic motion24. The enhanced catalytic efficiency and inhibitor binding specificity of *Ec*MTAN may also involve the full dynamic architecture of the protein.

Biological effectiveness of MTAN inhibitors in the context of the cell was measured in cell lysates of a virulent strain of *Vibrio cholerae* (N16961) grown in the presence of inhibitors. Direct measurements of MTAN activity that yielded nanomolar IC_{50} values for MT-, EtT-, and BuT-DADMe-ImmA demonstrate cell permeability for the inhibitors, most notably in the case of BuT-DADMe-ImmA. Despite having a 3-fold lower affinity with purified *Vc*MTAN, BuT-DADMe-ImmA inhibited cellular *Vc*MTAN activity 5-fold better than its MT-, and EtT- counterparts (Table 1). Although tightly bound *in vitro*, BuT-DADMe-ImmA inhibition of *Vc*MTAN activity in the cell required a 30-fold increase above the K_i^*, suggesting a significant diffusion barrier. With MT-, and EtT-DADMe-ImmA, the diffusion barrier required a gradient close to 500-fold above K_i^* to inhibit *Vc*MTAN in growing cells.

Despite the significant diffusion barrier, all three MTAN transition state analogues were potent inhibitors of autoinducer production in *V. cholerae* N16961, inhibiting quorum sensing induction in both *V. harveryi* reporter strains.

The role of quorum sensing in enterohemorrhagic *E. coli* O157:H7 EDL933 has also been extensively studied25–27. It is a highly pathogenic strain of *E. coli* that causes mortality and morbidity in vulnerable populations by producing Shiga toxins and lesions on intestinal epithelial cells. It uses autoinducers generated at high cell density to modulate concerted biological functions and succeed in host infection.

MT- and BuT-DADMe-ImmA are potent inhibitors of *E. coli* MTAN with dissociation constants of 2 and 0.3 pM, respectively18. Similar to results from *V. cholerae*, both MT- and BuT-DADMe-ImmA were able to cross the *E. coli* cellular membrane and cause nontoxic inhibition of AI-2 production. Interestingly, AI-2 inhibition in *E. coli* cells was not as efficient as in *V. cholerae* despite the fact that inhibition of *Ec*MTAN enzyme activity was at least 100-fold stronger than in *Vc*MTAN. A significant barrier to inhibitor permeability in *E. coli* may explain this discrepancy.

A concern in targeting MTAN to suppress quorum sensing is that overexpression of the quorum sensing pathway (or alternative pathways) might overcome the effect of MTAN inhibitors. Bacterial changes in gene expression in response to cellular signals generally occur rapidly, on the time scale of minutes to a few cell generation times. Serial transfer experiments showed that sensitivity towards BuT-DADMe-ImmA suppression of autoinducer-2 production was maintained in both *V. cholerae* N16961 and *E. coli* O157:H7 through progressive passaging of cells. This suggests that inhibition of quorum sensing was not only immediate, it also persisted for several generations.

Biofilm formation is an important bacterial strategy tightly linked to quorum sensing27,28. It is a vital survival mechanism for *Vibrio cholerae*, in both its infective and noninfective lifestyles29,30. The current model for *Vibrio cholerae* asserts that at high cell density in the abundance of autoinducers, biofilm formation is impaired by repression of the critical exopolysaccharide regulators HapR and c-di-GMP31,32. While most *Vibrio cholerae* El Tor strains possess a uniquely inverted quorum sensing mechanism to increase survival and infectivity32,33, the El Tor N16961 strain carries a natural frame-shift mutation in the *hapR* gene33,34 which abolishes repression on biofilm formation and cholera toxin production33. This makes it conceivable for biofilm formation to be suppressed by BuT-DADMe-ImmA under conditions that also inhibit autoinducer production in this strain.

In *E. coli*, it has been shown that autoinducer-2 added to cell cultures in microtiter plates increased biofilm formation 30-fold, and that a quorum sensing mutant produced 50% less biofilm than the isogenic wild-type strain35. As in the case of *V. cholerae* N16961, biofilm formation in *E. coli* O157:H7 was suppressed by an MTAN inhibitor that disrupts quorum sensing.

Transition state theory has been useful in the development of powerful inhibitors with *in vivo* effects against target enzymes. MT-, EtT-, and BuT-DADMe-ImmA are transition state analogues of bacterial MTANs and they show high potency in disrupting quorum sensing molecules in pathogenic strains of *Vibrio cholerae* and *Escherichia coli. Streptococcus pneumoniae*, *Neisseria meningitidis*, *Klebsiella pneumoniae*, *Staphylococcus aureus*, *Helicobacter pylori*, are some of the most aggressive human pathogens, and published evidence supports quorum sensing as promoting pathogenesis in these species7,36–40. Each of these bacterial species expresses MTAN and the transition state analogues described here are potent in inhibiting purified MTANs from these sources18,20,21. The potential of inhibiting quorum sensing by targeting MTAN is expected to extend to other pathogens beyond *V. cholerae* and *E. coli*.

METHODS

[8-^{14}C]MTA, DADMe-ImmucillinAs

[8-^{14}C]MTA and DADMe-ImmucillinAs were synthesized as described previously9,17

*Vc*MTAN expression and purification

*Vc*MTAN was expressed in *E. coli* as a His-tagged recombinant protein as described in Supplementary Methods online.

*Vc*MTAN kinetics and inhibition

Kinetic constants were determined by following loss of MTA at 274 nm ($\Delta\varepsilon_{274}$ = 1.6 $mM^{-1}cm^{-1}$). Reactions were carried out at 25 °C in 100 mM HEPES, pH 7.5, and 50 mM KCl at various MTA concentrations, and initiated by 10 – 12 nM *Vc*MTAN. Inhibition constants (K_i and K_i^*) were obtained using a xanthine oxidase-coupled reaction described previously18. Reaction mixtures contained 1 – 2 mM MTA, and various concentrations of MT-, EtT-, and BuT- DADMe-ImmA. Samples were prepared at standard buffer conditions, with ~0.5 units of xanthine oxidase (Sigma), and 12 nM *Vc*MTAN to initiate the reaction at 25 °C, monitored on a UV-Vis spectrophotometer at 293 nm. Inhibition constants were obtained using equation (1) for competitive inhibition using KaleidaGraph 3.6 (Synergy Software):

$$\nu_s'/\nu_s = \frac{K_m + [S]}{K_m + [S] + K_m[I]/K_d} \quad (1)$$

where ν_s' and ν_s are steady state with and without inhibitor, respectively; K_m is the Michaelis constant for MTA; [S] and [I] are the concentrations of MTA and inhibitor, respectively. If the concentration of inhibitor is less than ten times the concentration of enzyme, equation (2) was used for correction:

$$I' = I - (1 - \nu_0'/\nu_0)E_t \quad (2)$$

where I′ is the effective inhibitor concentration; I is the inhibitor concentration used in the assay; ν_0' and ν_0 are initial rates with and without inhibitor, respectively; and E_t is total MTAN concentration.

Crystallization of the BuT-DADMe-ImmucillinA-MTAN complex

Purified *Vc*MTAN was concentrated to 15 mg mL^{-1}, incubated with 1 mM BuT-DADMe-ImmA, and crystallized using sitting drop vapor diffusion at 18 °C against an 80 μL reservoir containing 0.2 M potassium iodide 20% (w/v) PEG3350, where 1 μL of the protein solution was mixed with 1 μL of the reservoir solution.

Data collection

Crystals were soaked in mother liquor supplemented with 20% glycerol and cooled to −178 °C prior to data collection, which was done subsequently at beamline X29A at the National Synchrotron Lightsource, Brookhaven National Laboratory using an ADSC Quantum 315

detector and 1.10010 Å wavelength. Each frame was exposed for 10 s with an oscillation range of 1°. The HKL2000 suite was used for integration and scaling of the data (Supplementary Table 2 online)41.

Structure determination and refinement

The structure of *Vc*MTAN- BuT-DADMe-ImmA complex was solved by molecular replacement using *E. coli* MTAN (PDB code 1Z5P. pdb without water) as search model. Molecular replacement with MOLREP, and refinement with REFMAC5 were done using the CCP4i package42–44. COOT was used for molecular modeling45. Clear density was observed in the Fo – Fc maps for the ligands at 3.5σ and were built into the electron density. Majority of the residues (89%) are located in the most favored region of the Ramachandran plot, while the remaining 11% are in the allowed region. Data processing and refinement statistics are summarized in Supplementary Table 2 online. All figures were made using PyMOL46.

Inhibition of cellular MTAN activity

V. cholerae N16961 (ATCC) was grown at 37 °C to stationary phase in LB medium for 16 hours with and without 1 – 1000 nM MT-, EtT-, and BuT-DADMe-ImmA. Cells were washed twice with PBS and lysed with BugBuster Reagent (Novagen). Cleared lysate was incubated with [8-^{14}C]MTA in 50 mM phosphate buffer, pH 7.9, 10 mM KCl at 25 °C for 20 minutes and quenched with perchloric acid to 20% final concentration. Reaction components were separated using reverse-phase HPLC as detailed in Supplementary Methods online, and MTAN activity was evaluated based on ^{14}C-adenine counts.

Autoinducer assay

Autoinducers secreted by *V. cholerae* N16961 treated with inhibitors were measured using *Vibrio harveyi* bioluminescence assay47 (described in Supplementary Methods online), where reporter *V. harveyi* strains produce light in response to autoinducers in *V. cholerae* spent media. The magnitude of induction is taken as the ratio of light output induced by the *V. cholerae* filtrate relative to blank, and was plotted against inhibitor concentration, and fitted to equation (3) to obtain the IC_{50}:

$$y = y_0 - \frac{c[I]}{IC_{50} + [I]} \quad (3)$$

where y is the magnitude of induction at inhibitor concentration [I]; y_0 is magnitude of induction without inhibitor (untreated sample); c is the maximum difference between treated and untreated sample, and IC_{50} is the inhibitor concentration representing half maximal induction. Average of at least six replicates was taken, with outliers greater than two standard deviations removed from analysis.

Autoinducer-2 production was measured similarly for enterohemorrhagic *E. coli* O157:H7 EDL933 (ATCC) grown in autobioinducer medium with 5 – 500 nM MT- and BuT-DADMe-ImmA, as well as for an *E. coli* MTAN knockout strain without inhibitor treatment.

To evaluate the effects of prolonged incubation with BuT-DADMe-ImmA on the growth and autoinducer production of *V. cholerae* N16961 and *E. coli* O157:H7, initial cell culture of these strains was prepared from a 1:100 dilution of overnight seed grown in LB medium at 37 °C, with and without 1 and 2.5 μM BuT-DADMe-ImmA. Cells were grown to stationary phase and aliquots were taken for OD_{600} and autoinducer-2 assays. Treated and untreated cells were serially diluted from dense cultures into fresh media, and grown under the same conditions of growth and inhibitor concentration for 26 generations. Cultures were prepared in triplicate, and for the bioluminescence assay the average of 6 – 8 replicates was taken.

Biofilm assay

V. cholerae N16961 and *E. coli* O157:H7 were diluted 1:100 from overnight seed cultures grown in LB medium in sterile, nontreated 96-well plates48. The plates were covered and grown static for 24 hours at 25 °C with and without 1 μM BuT-DADMe-ImmA. After removing the cell suspension and measuring OD_{600}, the plates were rinsed and stained with crystal violet solution for ten minutes. Once the dye was removed and the plate rinsed, the stained biofilm was solubilized using 1:4 acetone: ethanol for *E. coli*, and DMSO for *V. cholerae*. The extent of biofilm formation was obtained from the OD_{570} values, and the average from at least six replicates was reported.

Accession code

The coordinates and structure factors of *Vc*MTAN-BuT-DADMe-ImmA complex are deposited in the protein data bank with accession code 3DP9.

Supplementary Material

Refer to Web version on PubMed Central for supplementary material.

Acknowledgments

The authors acknowledge R. H. Furneaux, G. B. Evans, D. H. Lenz, G. F. Painter, and P. C. Tyler of Industrial Research Laboratory, Inc. (Lower Hutt, New Zealand) for supplying the DADMe-Immucillins. M. G. Surette (University of Calgary) for providing *Vibrio harveyi* strains BB120 and BB170, C. Bradbeer (University of Virginia) for the *Escherichia coli* MTAN knockout, and NIH Grant GM41916 for funding.

References

1. Fuqua WC, Winans SC, Greenberg EP. Quorum sensing in bacteria: the LuxR-LuxI family of cell density-responsive transcriptional regulators. J Bacteriol. 1994; 176:269–275. [PubMed: 8288518]
2. Sperandio V. Novel approaches to bacterial infection therapy by interfering with bacteria-to-bacteria signaling. Expert Rev Anti Infect Ther. 2007; 5:271–276. [PubMed: 17402841]
3. Vendeville A, Winzer K, Heurlier K, Tang CM, Hardie KR. Making ‘sense’ of metabolism: Autoinducer-2, LuxS and pathogenic bacteria. Nat Rev Microbiol. 2005; 3:383–396. [PubMed: 15864263]
4. Cegelski L, Marshall GR, Eldridge GR, Hultgren SJ. The biology and future prospects of antivirulence therapies. Nat Rev Microbiol. 2008; 6:17–27. [PubMed: 18079741]
5. Winzer K, Williams P. Quorum sensing and the regulation of virulence gene expression in pathogenic bacteria. Int J Med Microbiol. 2001; 291:131–143. [PubMed: 11437336]

6. Stroeher UH, Paton AW, Ogunniyi AD, Paton JC. Mutation of luxS of Streptococcus pneumoniae affects virulence in a mouse model. Infect Immun. 2003; 71:3206–3212. [PubMed: 12761100]
7. Winzer K, et al. Role of Neisseria meningitidis luxS in cell-to-cell signaling and bacteremic infection. Infect Immun. 2002; 70:2245–2248. [PubMed: 11895997]
8. Harasawa H, et al. Chemotherapy targeting methylthioadenosine phosphorylase (MTAP) deficiency in adult T cell leukemia (ATL). Leukemia. 2002; 16:1799–1807. [PubMed: 12200696]
9. Basu I, et al. A transition state analogue of 5′-methylthioadenosine phosphorylase induces apoptosis in head and neck cancers. J Biol Chem. 2007; 282:21477–21486. [PubMed: 17548352]
10. Singh V, Lee JE, Nunez S, Howell PL, Schramm VL. Transition state structure of 5′-methylthioadenosine/S-adenosylhomocysteine nucleosidase from Escherichia coli and its similarity to transition state analogues. Biochemistry. 2005; 44:11647–11659. [PubMed: 16128565]
11. Singh V, Schramm VL. Transition-state analysis of S-pneumoniae 5′-methylthioadenosine nucleosidase. J Am Chem Soc. 2007; 129:2783–2795. [PubMed: 17298059]
12. Singh V, Luo M, Brown RL, Norris GE, Schramm VL. Transition-state structure of Neisseria meningitides 5′-methylthioadenosine/S-adenosylhomocysteine nucleosidase. J Am Chem Soc. 2007; 129:13831–13833. [PubMed: 17956098]
13. Singh V, Schramm VL. Transition-state structure of human 5′-methylthioadenosine phosphorylase. J Am Chem Soc. 2006; 128:14691–14696. [PubMed: 17090056]
14. Balakrishnan K, Nimmanapalli R, Ravandi F, Keating MJ, Gandhi V. Forodesine, an inhibitor of purine nucleoside phosphorylase, induces apoptosis in chronic lymphocytic leukemia cells. Blood. 2006; 108:2392–2398. [PubMed: 16778146]
15. Robak T, Lech-Maranda E, Koerycka A, Robak E. Purine nucleoside analogs as immunosuppressive and antineoplastic agents: mechanism of action and clinical activity. Curr Med Chem. 2006; 13:3165–3189. [PubMed: 17168705]
16. Evans GB, Furneaux RH, Schramm VL, Singh V, Tyler PC. Targeting the polyamine pathway with transition-state analogue inhibitors of 5′-methylthioadenosine phosphorylase. J Med Chem. 2004; 47:3275–3281. [PubMed: 15163207]
17. Evans GB, et al. Second generation transition state analogue inhibitors of human 5′-methylthioadenosine phosphorylase. J Med Chem. 2005; 48:4679–4689. [PubMed: 16000004]
18. Singh V, et al. Femtomolar transition state analogue inhibitors of 5′-methylthioadenosine/S-adenosylhomocysteine nucleosidase from Escherichia coli. J Biol Chem. 2005; 280:18265–18273. [PubMed: 15749708]
19. Singh V, et al. Picomolar transition state analogue inhibitors of human 5′-methylthioadenosine phosphorylase and X-ray structure with MT-Immucillin-A. Biochemistry. 2004; 43:9–18. [PubMed: 14705926]
20. Singh V, et al. Structure and inhibition of a quorum sensing target from Streptococcus pneumoniae. Biochemistry. 2006; 45:12929–12941. [PubMed: 17059210]
21. Gutierrez JA, et al. Picomolar inhibitors as transition-state probes of 5′-methylthioadenosine nucleosidases. ACS Chem Biol. 2007; 2:725–734. [PubMed: 18030989]
22. Lee JE, et al. Structural rationale for the affinity of pico- and femtomolar transition state analogues of Escherichia coli 5′-methylthioadenosine/S-adenosylhomocysteine nucleosidase. J Biol Chem. 2005; 280:18274–18282. [PubMed: 15746096]
23. Bassler BL, Greenberg EP, Stevens AM. Cross-species induction of luminescence in the quorum-sensing bacterium Vibrio harveyi. J Bacteriol. 1997; 179:4043–4045. [PubMed: 9190823]
24. Saen-Oon S, Ghanem M, Schramm VL, Schwartz SD. Remote mutations and active site dynamics correlate with catalytic properties of purine nucleoside phosphorylase. Biophys J. 2008; 94:4078–4088. [PubMed: 18234834]
25. Anand SK, Griffiths MW. Quorum sensing and expression of virulence in Escherichia coli O157:H7. Int J Food Microbiol. 2003; 85:1–9. [PubMed: 12810266]
26. Sperandio V, Mellies JL, Nguyen W, Shin S, Kaper JB. Quorum sensing controls expression of the type III secretion gene transcription and protein secretion in enterohemorrhagic and enteropathogenic Escherichia coli. Proc Nat Acad Sci USA. 1999; 96:15196–15201. [PubMed: 10611361]

27. Li J, et al. Quorum sensing in Escherichia coli is signaled by AI-2/LsrR: effects on small RNA and biofilm architecture. J Bacteriol. 2007; 189:6011–6020. [PubMed: 17557827]
28. Herzberg M, Kaye IK, Peti W, Wood TK. YdgG (TqsA) controls biofilm formation in Escherichia coli K-12 through autoinducer 2 transport. J Bacteriol. 2006; 188:587–598. [PubMed: 16385049]
29. Zhu J, Mekalanos JJ. Quorum sensing-dependent biofilms enhance colonization in Vibrio cholerae. Dev Cell. 2003; 5:647–656. [PubMed: 14536065]
30. Matz C, et al. Biofilm formation and phenotypic variation enhance predation-driven persistence of Vibrio cholerae. Proc Nat Acad Sci USA. 2005; 102:16819–16824. [PubMed: 16267135]
31. Hammer BK, Bassler BL. Quorum sensing controls biofilm formation in Vibrio cholerae. Mol Microbiol. 2003; 50:101–114. [PubMed: 14507367]
32. Waters CM, Lu W, Rabinowitz JD, Bassler BL. Quorum sensing controls biofilm formation in Vibrio cholerae through modulation of cyclic di-GMP levels and repression of vpsT. J Bacteriol. 2008; 190:2527–2536. [PubMed: 18223081]
33. Zhu J, et al. Quorum-sensing regulators control virulence gene expression in Vibrio cholerae. Proc Natl Acad Sci USA. 2002; 99:3129–3134. [PubMed: 11854465]
34. Joelsson A, Liu Z, Zhu J. Genetic and phenotypic diversity of quorum-sensing systems in clinical and environmental isolates of Vibrio cholerae. Infect Immun. 2006; 74:1141–1147. [PubMed: 16428762]
35. Gonzalez Barrios AF, et al. Autoinducer 2 controls biofilm formation in Escherichia coli through a novel motility quorum-sensing regulator (MqsR, B3022). J Bacteriol. 2006; 188:305–316. [PubMed: 16352847]
36. Surette MG, Bassler BL. Quorum sensing in Escherichia coli and Salmonella typhimurium. Proc Nat Acad Sci USA. 1998; 95:7046–7050. [PubMed: 9618536]
37. Dunny GM, Leonard BAB. Cell-cell communication in gram-positive bacteria. Annu Rev Microbiol. 1997; 51:527–564. [PubMed: 9343359]
38. Balestrino D, Haagensen JAJ, Rich C, Forestier C. Characterization of type 2 quorum sensing in Klebsiella pneumoniae and relationship with biofilm formation. J Bacteriol. 2005; 187:2870–2880. [PubMed: 15805533]
39. Joyce EA, et al. LuxS is required for persistent Pneumococcal carriage and expression of virulence and biosynthesis genes. Infect Immun. 2004; 72:2964–2975. [PubMed: 15102809]
40. Rader BA, Campagna SR, Semmelhack MF, Bassler BL, Guillemin K. The quorum-sensing molecule autoinducer 2 regulates motility and flagellar morphogenesis in Helicobacter pylori. J Bacteriol. 2007; 189:6109–6117. [PubMed: 17586631]
41. Otwinowski, Z.; Minor, W. Processing of X-ray diffraction data collected in oscillation mode. In: Carter, CWJ.; Sweet, RM., editors. Methods Enzymol. Vol. 276. Academic Press; New York: 1997. p. 307-326.
42. Potterton E, Briggs P, Turkenburg M, Dodson E. A graphical user interface to the CCP4 program suite. Acta Crystallogr D Biol Crystallogr. 2003; 59:1131–1137. [PubMed: 12832755]
43. Vagin A, Teplyakov A. MOLREP: an automated program for molecular replacement. J Appl Cryst. 1997; 30:1022–1025.
44. Murshudov GN, Vagin AA, Dodson EJ. Refinement of macromolecular structures by the maximum-likelihood method. Acta Crystallogr D Biol Crystallogr. 1997; 53:240–255. [PubMed: 15299926]
45. Emsley P, Cowtan K. Model-building tools for molecular graphics. Acta Crystallogr D Biol Crystallogr. 2004; 60:2126–2132. [PubMed: 15572765]
46. DeLano, WL. The PyMOL Molecular Graphics System. DeLano Scientific; Palo Alto, CA, USA: 2002.
47. Greenberg EP, Hastings JW, Ulitzur S. Induction of luciferase synthesis in Beneckea harveyi by other marine bacteria. Arch Microbiol. 1979; 120:87–91.
48. O'Toole, GA., et al. Genetic approaches to study of biofilms. In: Doyle, RJ., editor. Methods Enzymol. Vol. 310. Academic Press; New York: 1999. p. 91-109.
49. Parsek MR, Val DL, Hanzelka BL, Cronan JE, Greenberg EP. Acyl homoserine-lactone quorum-sensing signal generation. Proc Nat Acad Sci USA. 1999; 96:4360–4365. [PubMed: 10200267]

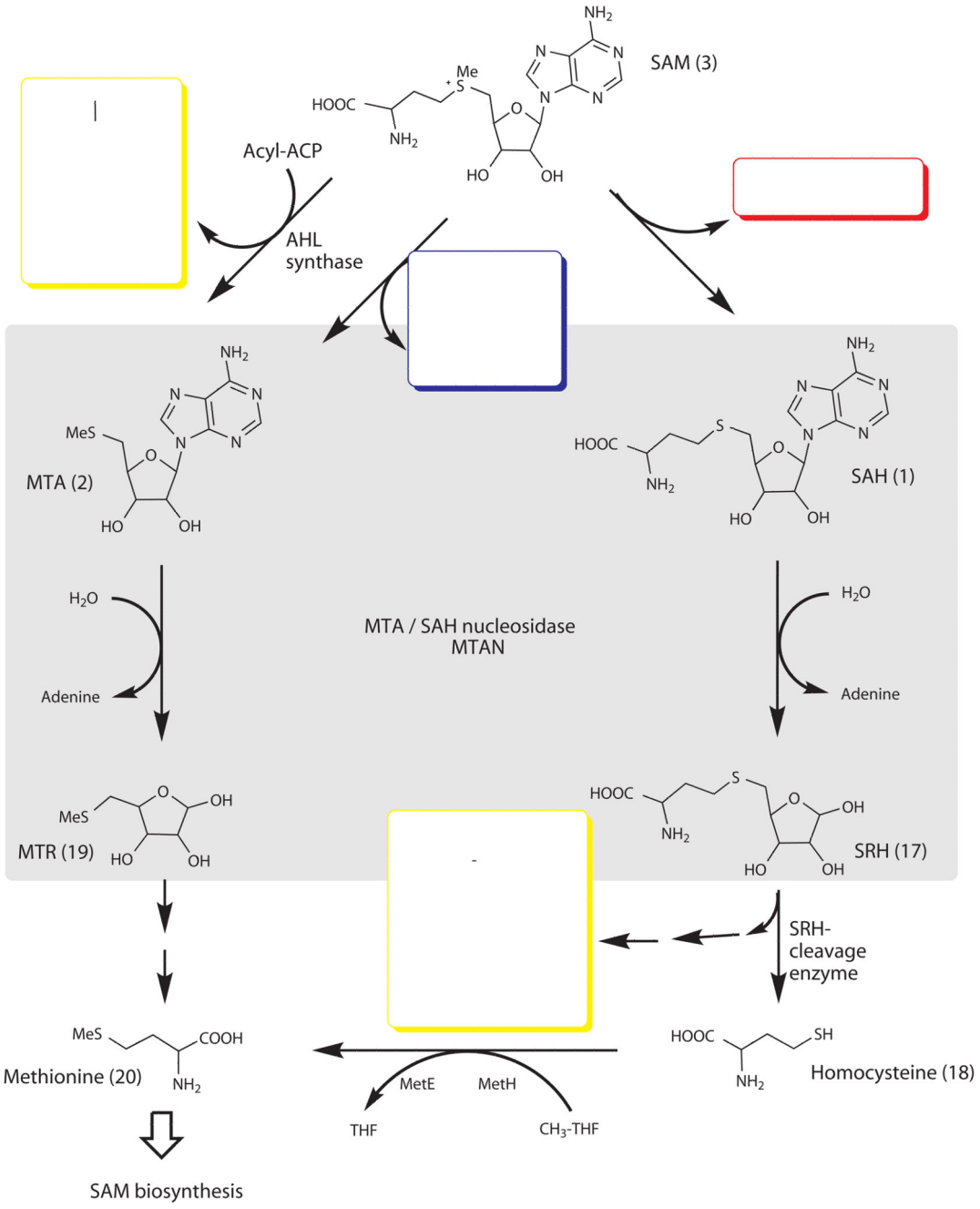

Figure 1.

Role of MTAN in bacterial utilization of *S*-adenosylmethionine (SAM). The scheme shows the pathways connecting DNA methylation (red box), polyamine synthesis (blue box), autoinducer production (yellow box), and methionine and adenine salvage. AHL synthase catalyzes the transfer of the amino acid moiety of SAM to an acyl acceptor to produce homoserine lactones in the synthesis of AI-1 molecules, and MTA as byproduct. In methyltransferase reactions, SAM produces SAH which is a precursor in the tetrahydrofuran synthesis of AI-2 molecules (shown here as furanosyl boron diester, **14**). Blocking MTAN

activity is expected to cause accumulation of MTA, resulting in product inhibition of AI-1 production by AHL synthase49. In addition, inhibition of MTAN can directly block the formation of *S*-ribosylhomocysteine (SRH, **15**), the precursor of AI-2. AI-1 and AI-2 are autoinducers used in bacterial quorum sensing, and MTAN offers a means to block formation of these signaling molecules.

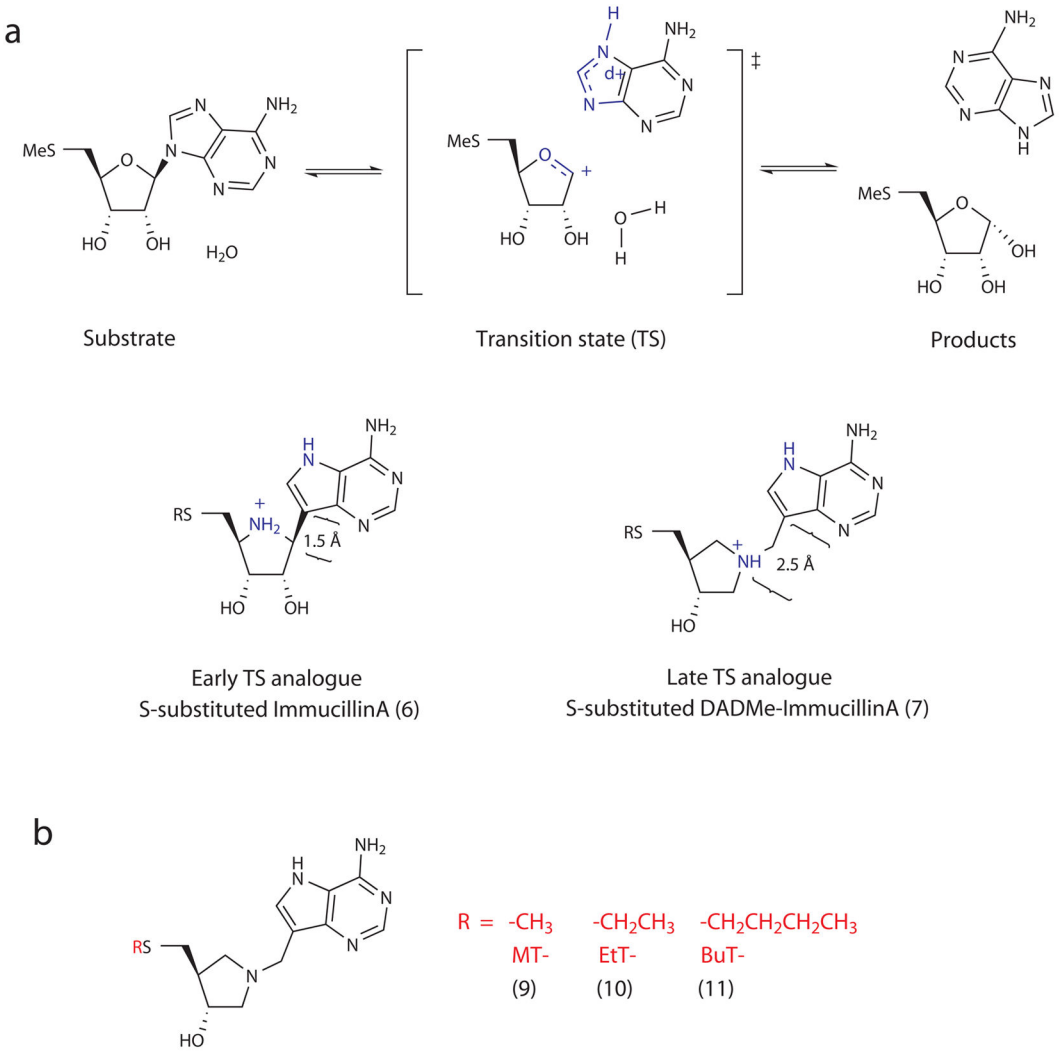

Figure 2.

The reaction catalyzed by MTAN with MTA as substrate. (**a, top**) shows a dissociative transition state for *E. coli* with ribooxacarbenium ion character10. Structures of stable analogues for an early dissociative transition state (ImmucillinA), and a late dissociative transition state (DADMe-ImmucillinA) depict differences in bond distances between the adenine leaving group and the ribosyl group, as well as charge localization (**a, bottom**). (**b**) Shown is the structure of *S*-substituted DADMe-ImmucillinA, along with MT-, EtT- and BuT- substituents.

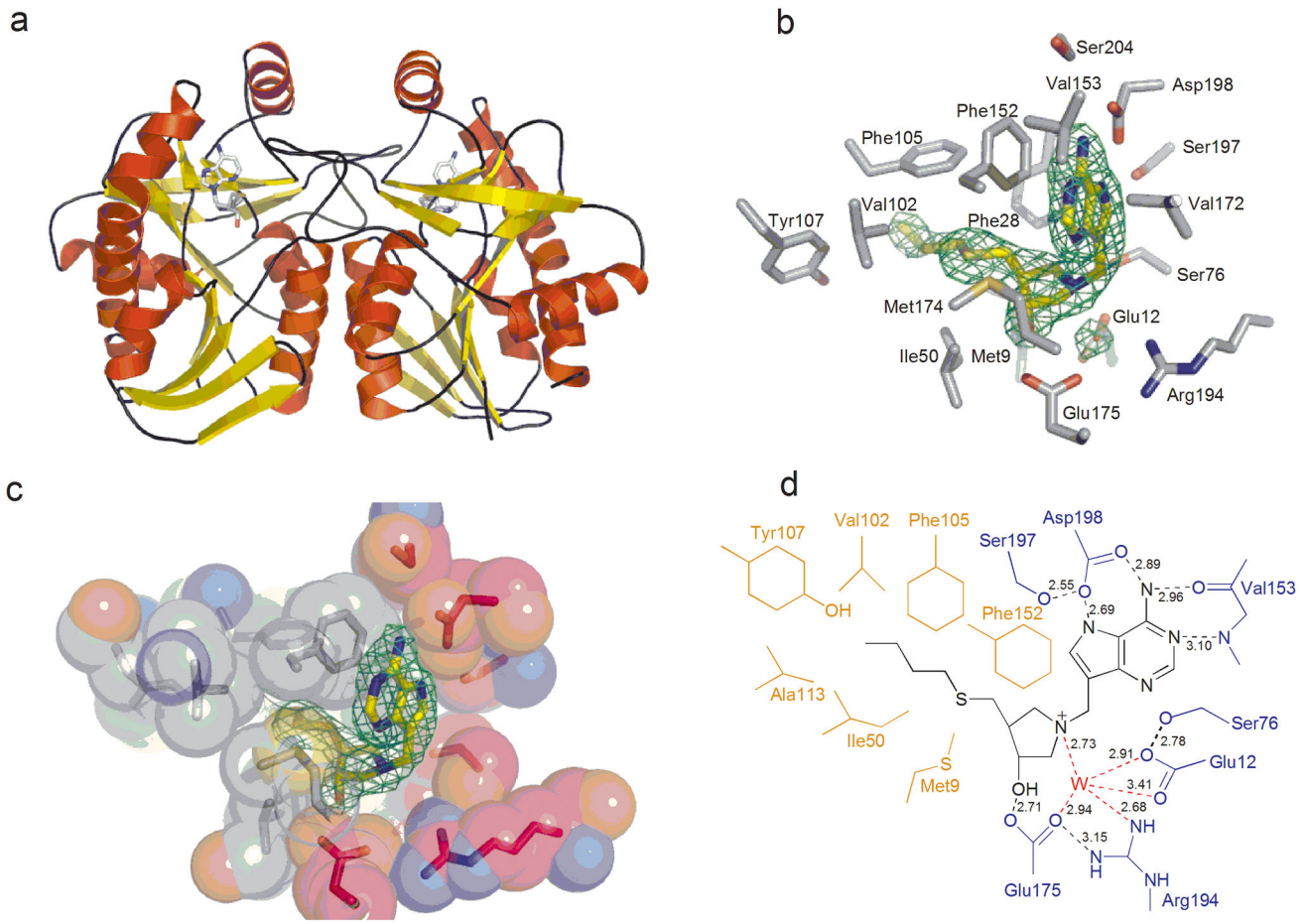

Figure 3.

Crystal structure of *Vc*MTAN in complex with BuT-DADMe-ImmA. (**a**) Overall structure of the *Vc*MTAN structure showing the asymmetric unit content with the inhibitor BuT-DADMe-ImmA bound in the active sites. (**b**) The active site of the *Vc*MTAN with a 2Fo − Fc map contoured at 1.2σ surrounding the BuT-DADMe-ImmA inhibitor and the proposed nucleophilic water molecule. (**c**) Space filling picture of the active site of *Vc*MTAN with BuT-DADMe-ImmA in the active site. Grey represents hydrophobic regions of the protein which interact with hydrophobic parts of the inhibitor. The red color shows parts of the protein that contain charged residues interacting with polar groups of the inhibitor, while green represents loop regions. (**d**) Schematic drawing of the BuT-DADMe-ImmA inhibitor bound in the active site of *Vc*MTAN showing catalytic contacts.

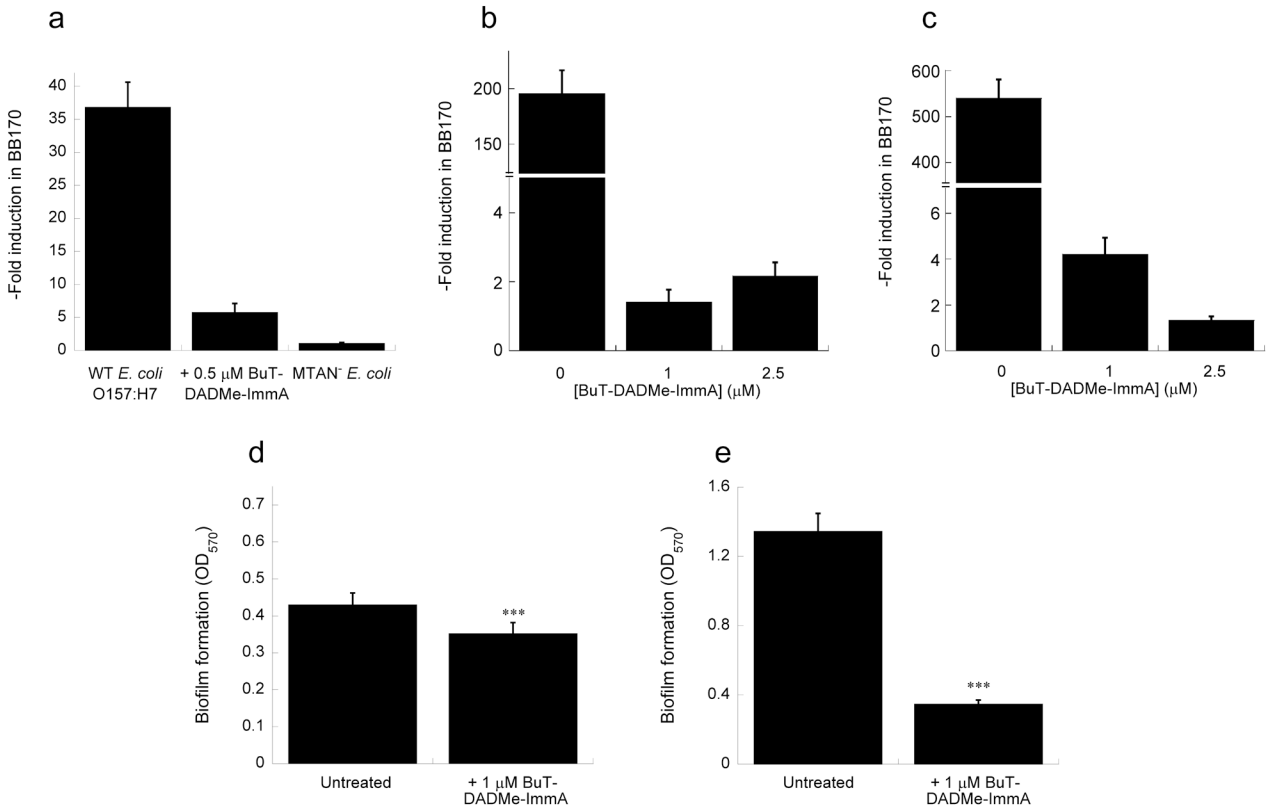

Figure 4.

Effect of BuT-DADMe-ImmA on autoinducer-2 production in pathogenic *E. coli* and *V. cholerae* upon short-term and long-term inhibitor treatment, and on static biofilm formation. (**a**) *E. coli* O157:H7 ± 0.5 μM BuT-DADMe-ImmA, and an MTAN⁻strain were grown static in AB medium for >5 generations before assaying the spent medium for autoinducer-2 production. (**b**) *E. coli* O157:H7, and (**c**) *V. cholerae* N16961 grown shaken in LB for 26 generations, and autoinducer-2 in the spent media was measured. Cultures were prepared in triplicate, and data represent mean values ± s.d. from at least 6 replicates. Biofilm formation studies on (**d**) *E. coli* O157:H7, and (**e**) *V. cholerae* N16961, ± 1 μM BuT-DADMe-ImmA grown static in LB medium at 25 °C for 24 hours on 96-well format. The observed difference in biofilm formation due to BuT-DADMe-ImmA was statistically significant at $t = 5.044$, ***$p < 0.001$, d.f. = 14 for *E. coli*; and $t = 26.689$, $p < 0.001$, d.f. = 14 for *V. cholerae*.

Table 1

Inhibition constants for purified MTAN activity, cellular MTAN activity, and autoinducer (AI) production determined as described in METHODS.

R-group	Purified enzyme inhibition K_i^*, pM	Cellular MTAN Inhibition IC_{50}, nM	AI Inhibition IC_{50}, nM	
			BB170 (*ai*1$^-$*ai*2$^+$)	BB120 (*ai*1$^+$*ai*2$^+$)
MT- (**7**)	73 ± 5	27 ± 4	0.94 ± 0.13	10.5 ± 2.6
EtT- (**8**)	70 ± 4	31 ± 7	11.0 ± 2.0	14.0 ± 2.0
BuT- (**9**)	208 ± 46	6 ± 1	1.4 ± 0.3	1.0 ± 0.2